Supplementary Material

Orientationally Glassy Crystals of Janus Spheres

Shan Jiang,[§,a] Jing Yan,[§,a], Jonathan K. Whitmer,[a,b,d] Stephen M. Anthony,[c]

Erik Luijten,[d,e] and Steve Granick[a,b,c]

Departments of Materials Science and Engineering,[a] Physics,[b] and Chemistry[c]

University of Illinois, Urbana, IL 61801, USA

Department of Materials Science and Engineering[d] and Department of

Engineering Sciences and Applied Mathematics,[e] Northwestern University,

Evanston, IL 60208, USA

EXPERIMENTAL DETAILS. Silica spheres were rendered amphiphilic by modification of a method described previously [cf. Refs. [10] and [14] of the main text, and Fig. S1(a)]. A submonolayer of 2 μm silica particles (Tokuyama), pretreated with piranha solution, was deposited on a glass slide and dried by evaporation. Electron-beam evaporation was then used to deposit 2 nm titanium as adhesion layer, followed by 25 nm gold onto the exposed hemisphere, the bottom hemisphere being protected by shadowing. This procedure produced a hemispherical coating that is thickest at the top where the nominal thickness is measured [Fig. S1(b)], and tapers towards the Janus equator. The gold side was then rendered hydrophobic by exposure to an ethanol solution of *n*-octadecylthiol (2 mM) overnight. The thickness profile is not relevant to the current study; the interparticle interaction is determined by the hydrophobic surface coating. After rinsing with copious ethanol, the treated particles were removed from the glass

slide by sonication and collected in deionized water. To subsequently prepare two-dimensional crystals, a dilute suspension of these Janus particles was injected into a sample cell for optical microscopy. Density mismatch caused the particles to quickly sediment to the bottom but levitated by electrostatic repulsion from the substrate, which was then slightly tilted (~1º) overnight (~12 hours). Between multilayers at the lower end of the sample cell and a dilute phase at the upper end, an extended area of monolayer colloidal crystal formed readily. After slowly adding millimolar quantities of NaCl, the particles became effectively close-packed. These samples were left overnight again, which homogenized the ionic strength throughout the sample and allowed the lattice distance to reach equilibrium. With this slow sedimentation technique, we were able to obtain single crystalline domains on the order of 50 particles on a side. For analysis, we selected only regions deep inside these single crystalline domains, usually roughly 20 particles on a side, regions without any positional defects. The resulting 2D crystals were then imaged under a Zeiss microscope in transmission mode using an air objective of 63× magnification (N.A. = 0.75), with 1.6× post-magnification. The images were captured using an Andor iXon EMCCD camera, usually at 10 frames/sec for fast dynamics or 1 frame/sec for long-time dynamics, for times up to 30 minutes. No aging was detectable during this time, as we confirmed by analyzing data at different stages of the time sequences. We did observe aging after 2–3 days, which stands as an interesting observation for future study. For each salt concentration, four independent single crystalline areas were imaged and averaged for analysis.

IMAGE ANALYSIS. To infer positional order, a band-pass filter was applied to the Fourier transform (FT) of the raw image [Fig. S2(a)] to remove both low- and high-frequency components [Fig. S2(b)]. Inverse FT then showed the hexagonal positional order in real space [Fig. S2(c)]. After identifying the center of each particle using a conventional particle tracking code, the in-plane rotation angle was obtained by connecting this center with the center of the bright pixels of the image, mathematically defined as the centroid of that portion of the image (Ref. [16] of the main text), as shown schematically in Fig. S2(d). Positional order, quantified by the local sixfold bond-orientational order parameter $\langle \psi_6 \rangle$ (Refs. [17] of the main text), was found to increase monotonically as 0.88, 0.92, 0.94, 0.96, and 0.97 for the five salt concentrations (1.00 mM, 1.25 mM, 1.50 mM, 1.75 mM, and 2.00 mM, respectively). We picked crystalline regions without any positional defects; the values of $\langle \psi_6 \rangle$ less than unity reflected the thermal fluctuation of particles on an otherwise perfect hexagonal lattice. Such fluctuations are stronger for samples with lower salt concentrations. Occasionally, untreated (homogeneous) particles were observed as another type of defect in the hexagonal lattice, but they were rare, fewer than 0.1%.

Each particle was tagged with positional information $\mathbf{r}$ and orientational information $\hat{\mathbf{n}}$. We ignored the out-of-plane fluctuation of particles and only focused on the in-plane component $\hat{\mathbf{n}}$. This approximation is valid because for the relevant salt concentrations the directors of the particles are preferentially oriented in the x–y plane, to maximize the hydrophobic attraction. We then calculated various forms of spatial and temporal correlation functions following the standard procedures. The characteristic oscillations in $G(r)$ reflect the striped nature of the orientational order: neighboring

particles tend to point to each other, while two particles that are separated by twice the lattice constant a tend to point in the same direction. The lattice constant a increases with decreasing salt concentration. For simplicity, we normalized r by the lattice constant a for each salt concentration; as a result, the peak positions of $G(r)$ do not shift with salt concentration.

To characterize the local environment, we first identified the number of attractive bonds N_i for each particle i. An attractive bond is defined if both $\hat{\mathbf{n}}_i \cdot \hat{\mathbf{r}}_{ij} > 0$ and $\hat{\mathbf{n}}_j \cdot \hat{\mathbf{r}}_{ji} > 0$, where $\hat{\mathbf{r}}_{ij}$ is the unit vector pointing from particle i to particle j. The particle trajectories were then divided into pieces in which N_i stays unchanged. It is possible that a particle flips from one orientation to another while keeping N_i unchanged. However, since the configurations that permit this are rare, and the barriers between two such orientations are high (especially when the hydrophobic attractions are strong), such events contribute minimally to our characterization.

SIMULATION MODEL. Our model is informed by experimental data that shows interparticle spacing to be essentially independent of particle orientation. Thus, within the crystal, salt-dependent electrostatic repulsion combines with gravitational pressure to determine the average interparticle spacing, not affected by attractions between the hydrophobic hemispheres. However, as a consequence the ionic strength affects the effective magnitude of the hydrophobic attraction, since the latter exhibits an exponential dependence on separation (Refs. [23] and [24] of the main text). We model this via Monte Carlo (MC) simulations in which the particles are fixed on a lattice. These equilibrium positions alone model the electrostatic aspects of the system, leaving an

orientation-dependent potential to mimic the hydrophobic attraction. The reduced surface-to-surface distance d/λ, in which d is the surface-to-surface separation and λ the hydrophobic attraction range, determines the attraction $U(d) = U_0 e^{-d/\lambda}$, with U_0 = $-10k_BT$. The orientation dependence is modeled by a smooth boundary,

$$U\left(\hat{\mathbf{n}}_1, \hat{\mathbf{n}}_2, \hat{\mathrm{r}}_{12}, d\right) = U(d) f(\theta_1) f(\theta_2) \quad , \tag{S1}$$

where

$$f(\theta) = \begin{cases} 1 & \theta < \theta_{\text{cut}} - \theta_{\text{tail}} \\ 0 & \theta > \theta_{\text{cut}} + \theta_{\text{tail}} \\ \cos^2\left[\dfrac{\pi\left(\theta - \theta_{\text{cut}} - \theta_{\text{tail}}\right)}{4\theta_{\text{tail}}}\right] & \theta_{\text{cut}} - \theta_{\text{tail}} < \theta < \theta_{\text{cut}} + \theta_{\text{tail}} \end{cases} \tag{S2}$$

and

$$\theta_i = \cos^{-1}\left(\hat{\mathbf{n}}_i \cdot \hat{\mathbf{r}}_{ij}\right) . \tag{S3}$$

Here, $\hat{\mathbf{n}}_i$ is the orientation of particle i, and $\hat{\mathbf{r}}_{ij}$ is the normalized center-to-center vector of the two neighboring particles, pointing from particle *i* to particle *j*. The angles θ_{cut} and θ_{tail} in these simulations take the values 89.0º and 1.0º respectively, making the interaction very flat within its attractive domain (cf. Fig. S3). In reality, some local structure exists when hydrophobic sides face each other owing to fluctuation of the position of the particles or variation in the film thickness resulting from the directional evaporation; such effects are not captured in this model, since we focus on the global dynamics. Simulations take place on an $N \times N$ rhombus ($N = 50$) with periodic

boundary conditions mimicking an extended hexagonal crystal. Canonical spin rotation sweeps, in which N^2 trial moves are proposed to reorient a random particle, then proceed.

Data in the simulations are acquired from sequential outputs after an initial equilibration period of 10^6 "fast" MC sweeps followed by 10^6 "slow" MC sweeps. The maximum absolute angular displacement in each trial move is $|\Delta\theta| = 60°$ for the fast steps and $|\Delta\theta| = 5°$ for the slow steps. A typical relaxation of the energy for each value is plotted in Fig. S4. The two types of sweeps are utilized to rapidly relax the system to a near-equilibrium state, and then to allow it to equilibrate further before data is taken. Each trajectory is followed for an additional 10^5 MC sweeps, using the same maximum displacement as the "slow" moves. As these are local rotations, meaningful dynamic information can be obtained from sequential states. Some representative images of the system at different d / λ are given in Fig. S5. Five independent runs are performed for each λ studied. An approximate mapping between the simulation and the experiment is achieved by noting that for a small change of salt concentration, d / λ scales inversely with the square root of salt concentration (Ref. [23] of the main text); this is utilized to connect MC dynamics with experiment (cf. Fig. 3 and related text in the main article).

Legends for Supplementary Movies

Supplementary Movie 1: Representative short-time dynamics of a two-dimensional Janus crystal at 2 mM NaCl. The movie is played in real time.

Supplementary Movie 2: Representative long-time dynamics of a two-dimensional Janus crystal at 2 mM NaCl, showing the overall pattern evolution. The true time difference between successive images is 1 minute.

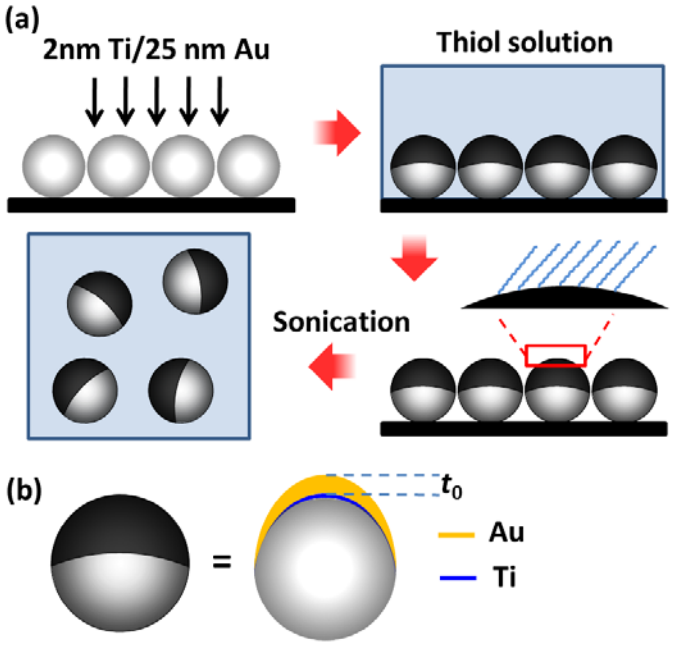

Figure S1: (a) Schematic representation of the synthesis of the amphiphilic Janus particles. (b) Schematic of the as-produced film geometry. Directional coating causes the film to be thickest at the top and taper towards the Janus equator, but subsequent coating with a hydrophobic monolayer produces uniformly hydrophobic interactions. The nominal thickness t_0 corresponds to the film thickness at the top.

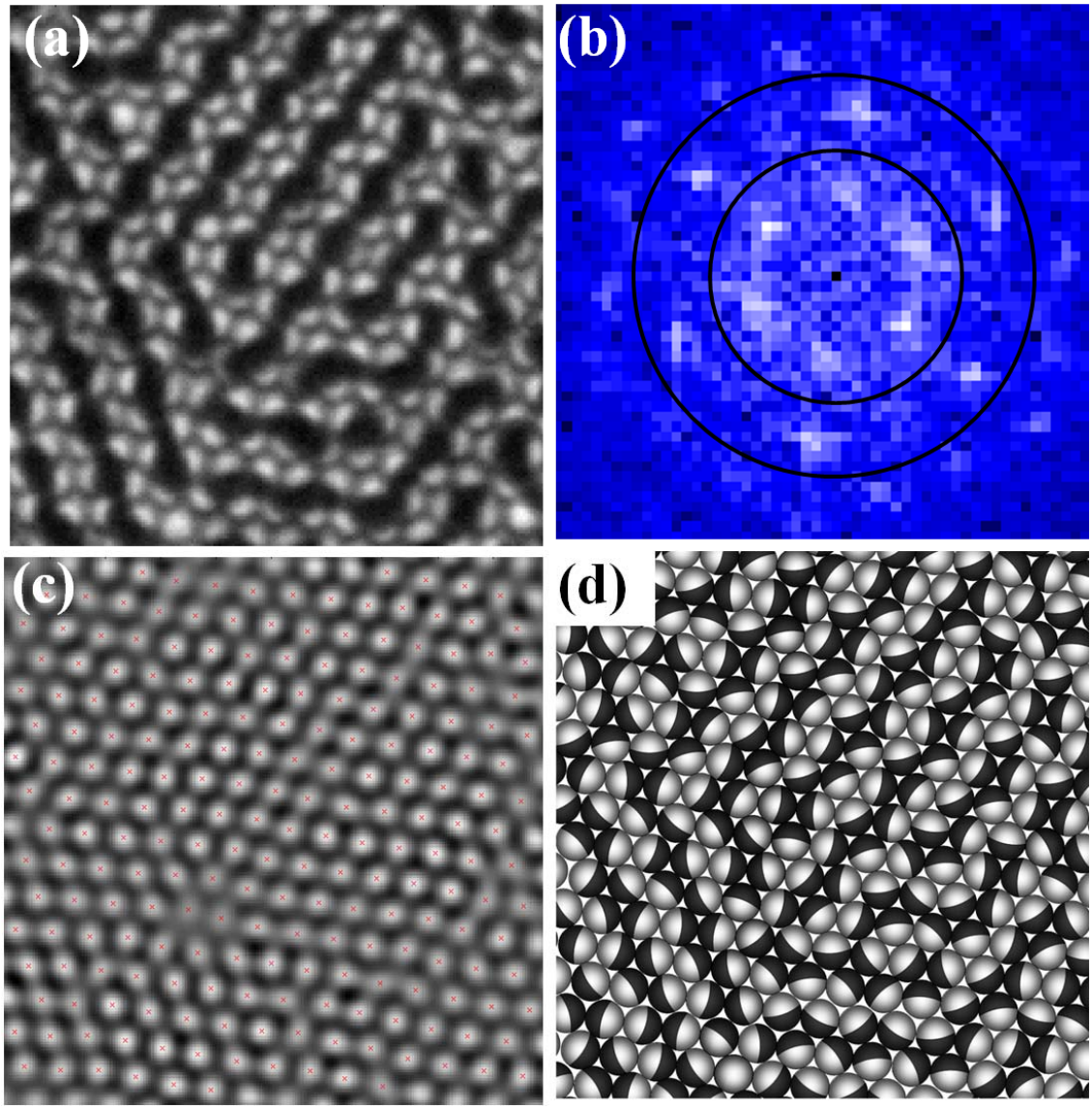

Figure S2: Image analysis process. (a) Raw image obtained at 2 mM NaCl. (b) Fourier transform of (a). The sixfold symmetry between the two concentric rings corresponds to hexagonal positional order. (c) Inverse Fourier transform of panel (b) after applying a band-pass filter. Red crosses indicate the particle centers determined by the tracking algorithm. (d) Reconstructed representation of the experimental image, including particle orientation.

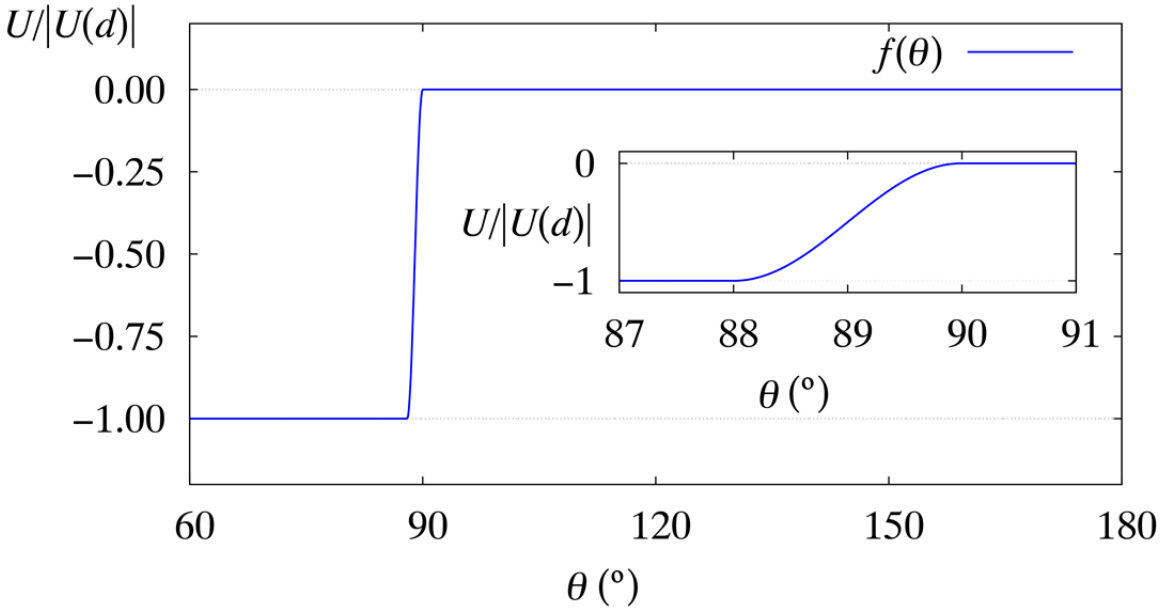

Figure S3: Angular dependence $f(\theta)$ [Eq. (S2)] of the orientation-dependent interaction potential used in the simulations. Inset: detail of the transition from attractive to non-interacting orientations.

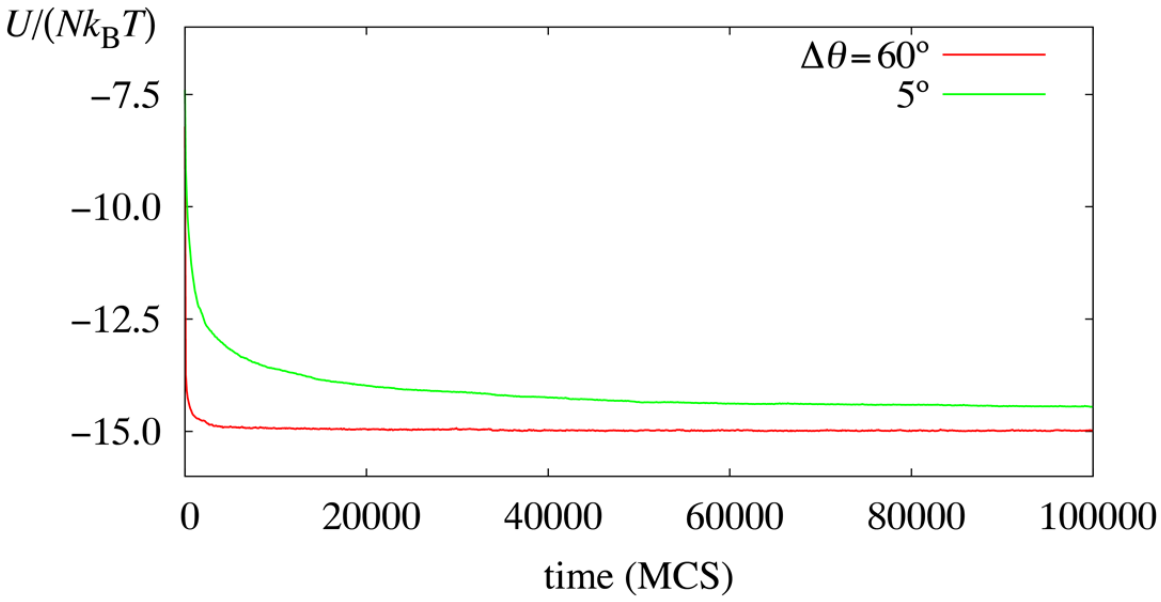

Figure S4: Relaxation of the energy per particle in the simulation model with $d = 0$ and $U_0 = -10k_BT$. Each particle has an average of three bonds with other particles, each of which contributes $-5\,k_BT$ per particle, leading to a ground state of $-15\,k_BT$ per particle. Large attempted displacements $\Delta\theta$ relax the system more efficiently, whereas smaller displacements are more abundant experimentally, justifying our two-step approach to equilibration to first quench the system and then explore the local dynamics.

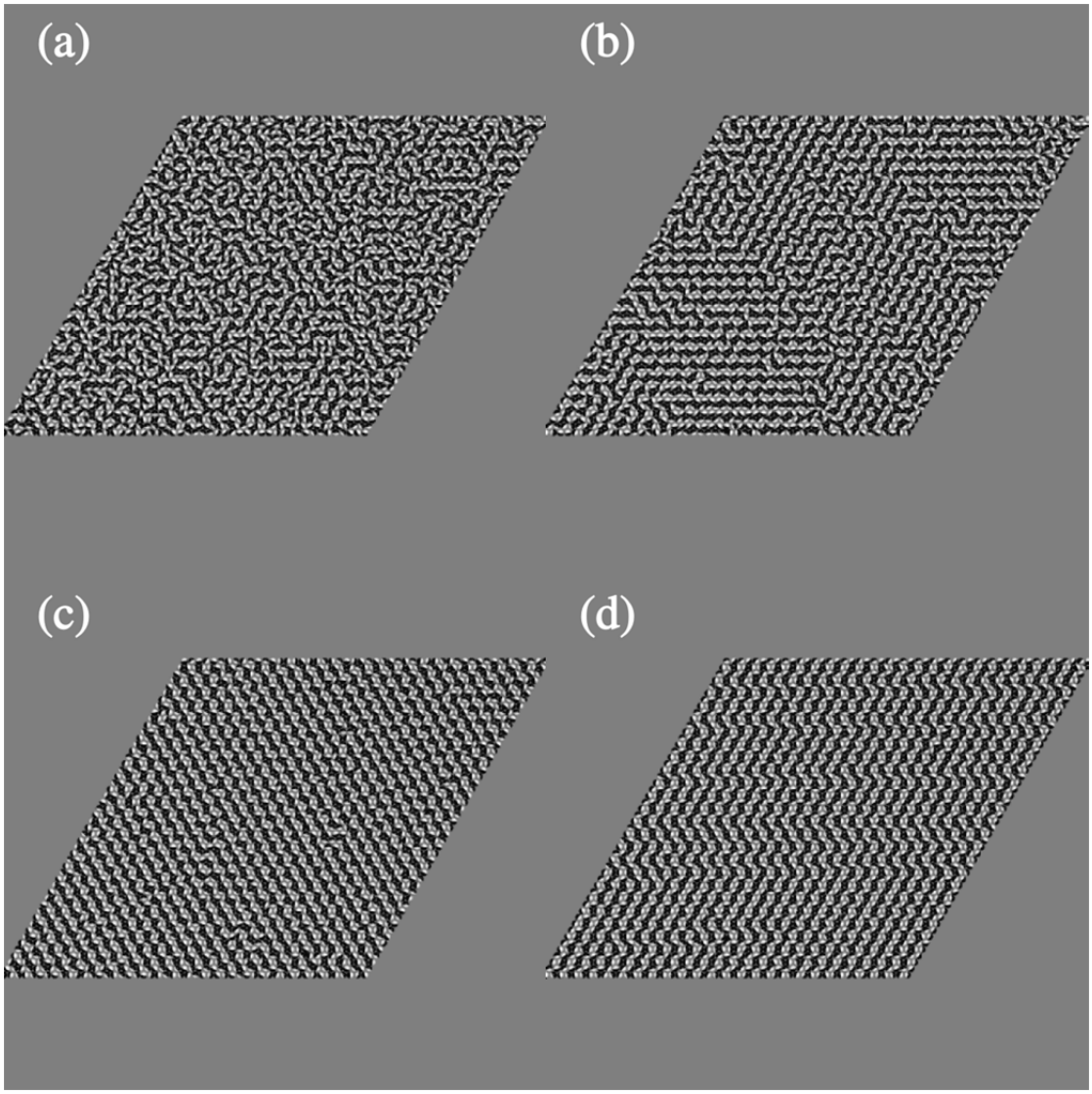

Figure S5: Representative configurations with (a) $d/\lambda = 3$, (b) $d/\lambda = 2$, (c) $d/\lambda = 1$, (d) $d/\lambda = 0$. Note that decreasing d/λ strengthens the effective hydrophobic attraction, promoting the formation of ordered stripes.

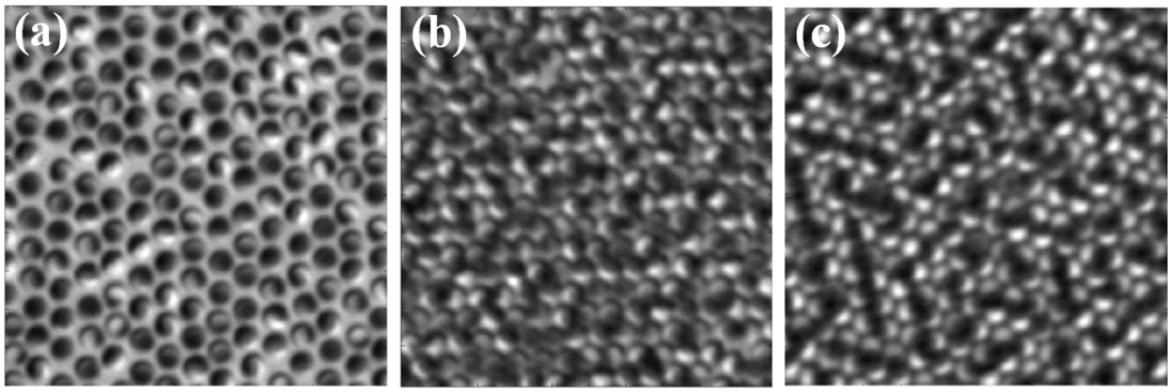

Figure S6: Representative experimental images at different salt concentrations. (a) No salt added; (b) 1.00 mM NaCl; (c) 1.50 mM NaCl.

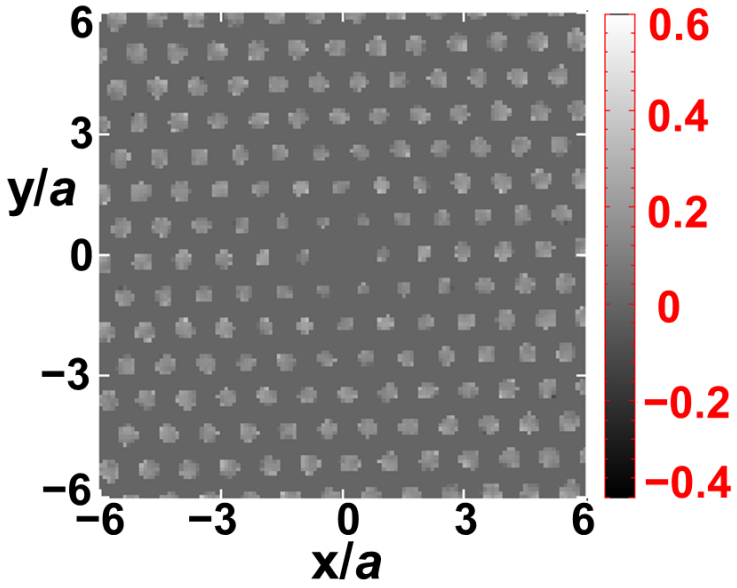

Figure S7: Static angular correlation $G(\mathbf{r}) = \langle \hat{\mathbf{n}}(0) \cdot \hat{\mathbf{n}}(\mathbf{r}) \rangle$ in a sample with moderate salt concentration (1.50 mM). To compare with Fig. 2(a) in the main text, the same grey scaling is used. The diminished striped order compared to 2.00 mM reduces the contrast. However, one can still identify the slightly negative correlation for the first shell of neighbors, as well as a stronger positive correlation for the second shell, which is consistent with the radially averaged value shown in Fig. 2(b).

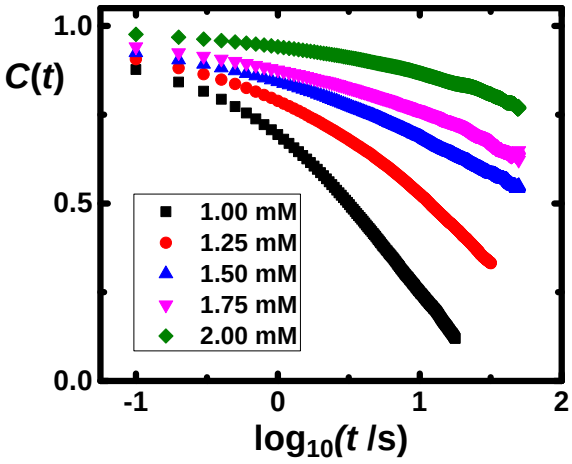

Figure S8: Single-particle angular autocorrelation function $C(t)$ for different salt concentrations, showing slower and more heterogeneous dynamics as salt concentration increases.

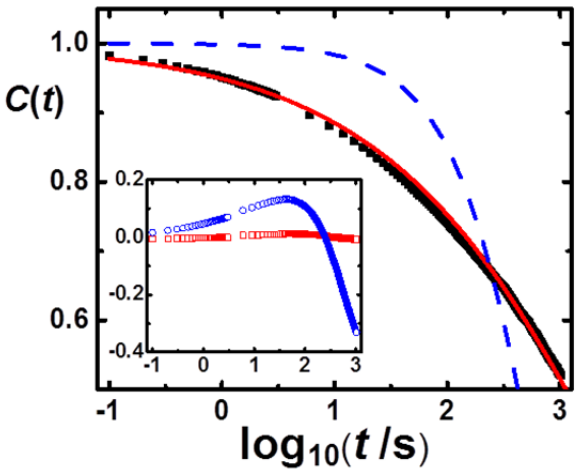

Figure S9: Comparison of a single exponential fit (blue dashed line) and a stretched exponential fit (red). Inset: residuals from the single exponential fit (blue) and the stretched exponential fit (red). It is clear that a single exponential cannot fit the data whereas a stretched exponential fits the entire range of data satisfactorily.